

# Design Features and Performance of a PET System for Animal Research

P. Duffy Cutler, Simon R. Cherry, Edward J. Hoffman, Ward M. Digby, and Michael E. Phelps

*Division of Nuclear Medicine and Biophysics, UCLA School of Medicine, Los Angeles, California and CTI PET Systems, Knoxville, TN*

The design features of a PET system designed for animal studies are described and its performance evaluated. The system employs a two-dimensional modular detector array consisting of bismuth germanate detector elements that are 3.5 mm (transaxially) by 6.25 mm (axially) by 30 mm (deep). These arrays are optically coupled to a pair of dual-photo-multiplier tubes (PMT). The detector ring is 64 cm in diameter with a field of view (FOV) of 40 cm by 5.4 cm axially, acquiring 15 slices at 3.4 mm spacing. These features include: (1) digitization of PMT signals from each block for improved position and energy discrimination of coincident events and (2) dual-window energy discrimination for simultaneous but separate acquisition of photopeak and scatter data. Intrinsic resolution averages 3.5 mm at the center of the FOV, while reconstructed resolution (ramp filter) ranges from 3.8 mm at the center of the FOV to 4.6 mm at an 8 cm radius. Axial resolution averages 4.4 and 4.9 mm and sensitivity averages 4.2 and 6.1 kcps/ $\mu$ Ci/cc for cross planes and enhanced direct planes, respectively. Randoms fraction is high due to reduced interplane shielding, giving a peak true count rate of 103 kcps for a 10 cm cylinder. Scatter as a fraction of trues is 16% for a 10 cm cylinder at a lower energy threshold of 350 keV. All parameters are sensitive to energy threshold. Spatial resolution improves by 11% transaxially and 9% axially, scatter fraction drops to 10%, and overall sensitivity drops by 48% when the threshold value is increased from 350 keV to 450 keV.

**J Nucl Med 1992; 33:595-604**

**P**rogress in the development of new tracer kinetic models and new radiopharmaceuticals for PET, through the use of animal research, has been hindered by the poor resolution of clinical PET systems relative to the size of the organ systems of most laboratory animals. The single-slice system of Derenzo et al. has the ability to resolve many of these small structures (1), but also has the practical limitation of being unable to examine more than a single slice in a dynamic study. A system has been built

for our laboratory by CTI/Siemens, Knoxville, TN, specifically for use in animal research.

This version of a block detector-based PET camera uses shorter septa to regain sensitivity and an improved system of energy discrimination to deal with the associated increase in scatter fraction. Event positioning is also handled in a novel way, giving rise to greater flexibility in optimizing detector performance. The design is specific for measuring in vivo processes in animals where the imaging cross section is generally smaller, giving rise to fewer accidental and scattered coincidences than in patient studies.

## SYSTEM DESCRIPTION

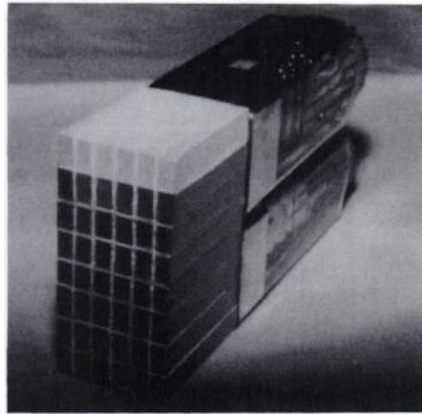
The CTI/Siemens Animal Tomograph (model 713) utilizes a single 64-cm diameter ring of 80 BGO "block" detectors collimated with seven annular, tungsten septa (Table 1). These septa, which are 6 cm deep by 0.5 mm thick, help define the system's 15 image planes at a 3.38 mm spacing. Each detector module contains a 25  $\times$  54 mm block of BGO segmented into a 6  $\times$  8 array of crystal elements 3.5 mm (transaxially) by 6.25 mm (axially). The crystal is coupled to two Hamamatsu R1548 dual photo-multiplier tubes (PMTs) whose four output channels are used with an Anger-type logic for detector identification (2-4). An example of one of these detector modules without its light-tight cover is shown in Figure 1. The system uses stationary data collection in which alternate projection angles are interleaved to yield an effective linear sampling distance of 2.1 mm (5).

## Front-end Electronics

The front-end electronics have been significantly modified (6) from previous CTI clinical PET systems (7) to implement a system of digital positioning and energy discrimination. Energy and position signals are digitized by a set of flash analog-to-digital converters (ADCs) immediately following the integration of the light from a scintillation event. This system allows the user to manipulate the detector identification and energy discrimination with software. Each set of four detector modules is grouped into a unit called a "bucket," which is controlled by an on-board processor, memory, and a 62.5 MHz synchronized clock. Each of the system's 20 buckets operates

Received Aug. 2, 1991; revision accepted Oct. 21, 1991.  
For reprints contact: Duffy Cutler, Div. of Nuclear Medicine and Biophysics, c/o Rm. B2-049 CHS, UCLA School of Medicine, Los Angeles, CA 90024.

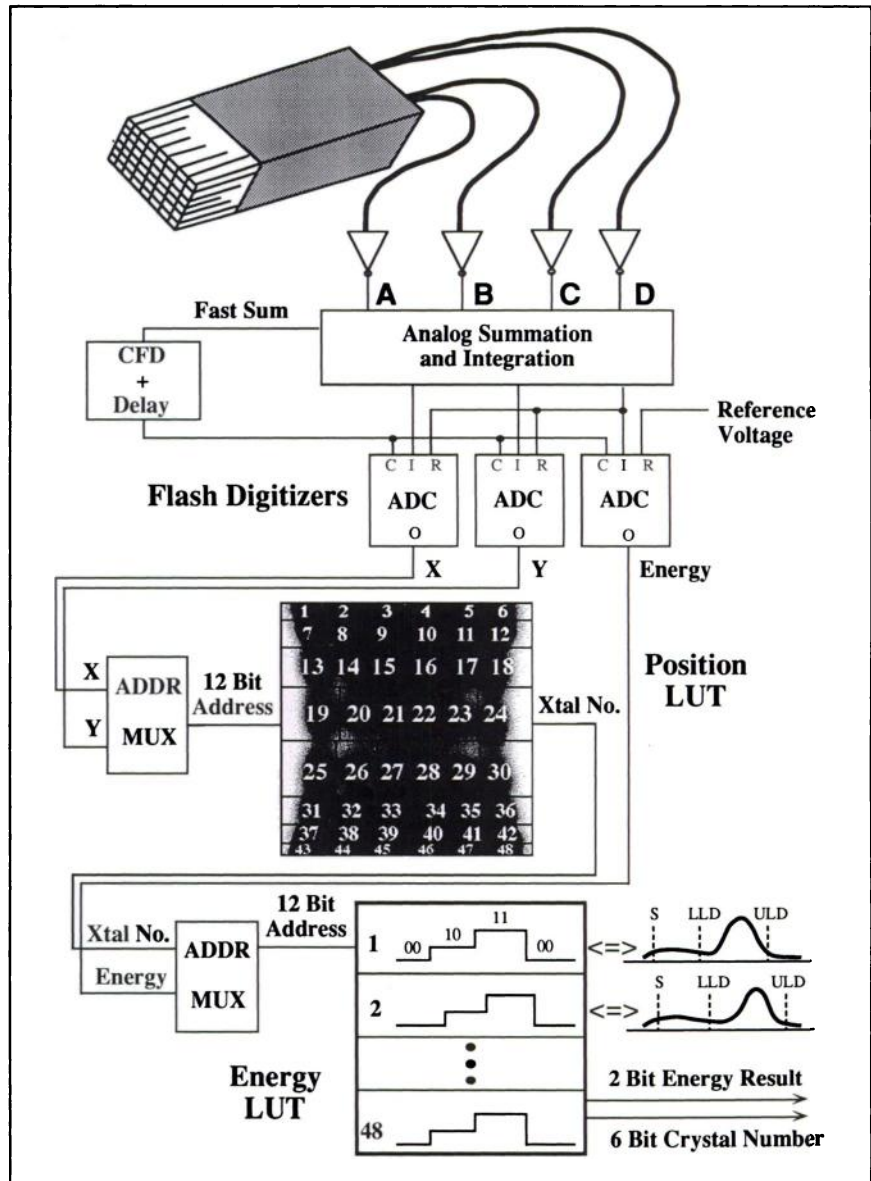
**FIGURE 1.** The detector module is a  $6 \times 8$  matrix of  $3.5 \times 6.25$  mm BGO crystals coupled to two Hamamatsu PMTs. Each PMT has two separate dynode chains within a common glass envelope. The resulting four anode signals enable an event to be localized to one of the 48 detector elements.



**TABLE 1**  
Physical Characteristics of the CTI 713

Detector size	$3.5 \times 6.25 \times 30$ mm
Detector spacing	4.1 mm c-c
PMTs	160 Hamamatsu R1548 Dual-Channel 2.54 cm square
Number of detectors	480 per ring $\times$ 8 rings
Ring diameter	64 cm
Patient port (FOV)	40 cm (32 cm)
Septa	7 Tungsten 0.5 mm $\times$ 6 cm

independently and synchronously in processing a single event during a 256-nsec interval, the basic sampling time of the system (8).



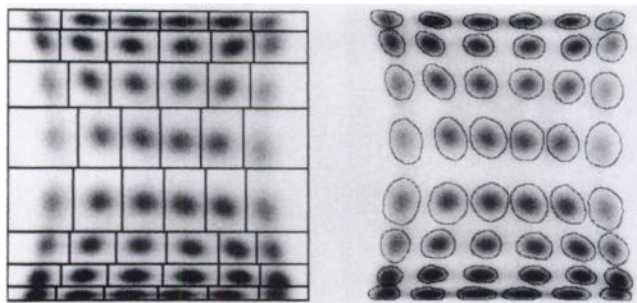
**FIGURE 2.** Schematic of front-end electronics. Position and energy look-up tables are accessed by direct addressing with digitized block outputs. The crystal number and 2-bit energy result are appended to the time stamp, block number and bucket number to form an address for the event.

Figure 2 provides a schematic diagram of the configuration of the front-end electronics. The microprocessor on the bucket controller can create and manipulate the lookup tables (LUTs) corresponding to each of its four blocks. During calibration, a block's position and energy responses are recorded as it is exposed to a uniform source. The position response is a histogram of 48 peaks in which single events have been positioned by two-dimensional Anger-type logic (2). In creating the positioning LUT, an algorithm executed by the bucket controller fits a grid of rectangular detector boundaries over the 48 peaks so as to achieve a rough balance of the number of events seen by each crystal. This set of boundaries and corresponding crystal numbers form a LUT which is stored and used during acquisition.

The energy spectrum of each crystal in each block is also measured during calibration to determine the pulse height of the photopeak relative to the six bits or 64 channels of the ADC. The energy LUT for each crystal is created by first calculating the valid region in the 64-channel spectrum corresponding to the photopeak, (a second "scatter" window can also be defined), and then loading a 2-bit code into each of the 64 addresses in the LUT. The first bit, called the "request bit," signifies if the event will be saved and processed further, while the second bit tags the event as a true event, if it is 1, or a "scattered" event, if it is 0. A crystal's valid energy region is determined from user-defined upper and lower level discriminator (LLD and ULD) values and an optional scatter discriminator value.

During acquisition, a detector's constant fraction discriminator (CFD) is triggered when a photon is absorbed, causing a 7-bit time stamp to be generated. This value indicates the photon's arrival time with respect to the current 256-nsec interval. The four PMT signals are integrated for roughly 0.5  $\mu$ sec, then combined to form an energy signal and two position signals (axial and transaxial). These are digitized on the delayed strobe of the CFD. The two position signals are combined to form a memory address pointing to a location in the previously-stored position LUT. This memory location will contain the number of the crystal most likely to have absorbed the photon. The crystal number and digitized energy signal form a second memory address for comparison with the energy LUT. If this address contains a valid 2-bit energy result, then a binning address is formed containing the time stamp, crystal number, block number, bucket number, and scatter bit to be sent to the coincidence processing electronics.

The positioning LUT has flexible detector boundaries that may be created and accessed with software. Inherent in the design is the ability to define valid regions of any shape to account for non-linearities in the positioning response, as well as "dead" regions, corresponding to ambiguous events that should be rejected. In the current implementation, however, the positioning LUT has no



**FIGURE 3.** Two possible forms of the positioning lookup table (LUT). Digitized x and y position signals form a  $64 \times 64$  response histogram. The LUT discriminates this response into one of the 48 regions which represent each crystal. (Left) The LUT is a grid of rectangular regions which will account for the nonlinearities inherent in the block but will also accept ambiguously placed events. (Right) Regions defined by lines of isoprobability create a more selective LUT. Both are determined empirically during the setup of the block with a flood source.

dead areas and assigns every valid event to one of the 48 detector elements. The set-up algorithm evaluates the flood response and uses a few simple rules to place rectangular detector boundaries in the valleys between the response peaks. Figure 3a shows an example of this type of LUT. Figure 3b is a more selective type, which rejects ambiguous events, thus improving spatial resolution, but at the expense of sensitivity.

## MATERIALS AND METHODS

### Sensitivity

Low count rate sensitivity of the 713 was measured using a 20-cm cylinder containing  $^{68}\text{Ge}$ - $^{68}\text{Ga}$  at an activity concentration of 0.084  $\mu\text{Ci/cc}$  of positron emitter. This measurement was performed for a standard data collection configuration (direct and cross-planes) and with a sensitivity-enhanced configuration. In the latter, the sensitivity of a direct plane is supplemented using two lines of response (LORs) between the ring above and the ring below the direct plane. Thus, "direct" planes consist of three axial LORs compared with the conventional single LOR. Sensitivity values for cross and enhanced direct planes were determined for LLD values of 250, 350 and 450 keV.

The sensitivity variation across an individual block was measured with a  $^{22}\text{Na}$  line source swept across the center of the field of view (FOV) in 0.5-mm steps. Count rates corresponding to specific detector pairs were extracted from the sinogram to give a detailed sensitivity response for typical detector pairs. These data also provide a measure of the intrinsic detector pair resolution.

Detailed sensitivity profiles of the imaging planes of the PET system were measured with a line source aligned transaxially which is moved axially through the FOV in 0.75-mm steps. Events measured in each plane were combined to produce a set of 15 axial line spread functions (LSFs) representing the slice profiles at a given radial distance. The LSFs were integrated to give the relative sensitivity of each plane.

High count rate performance was measured for the enhanced plane configuration with uniform cylinders of  $^{18}\text{F}$ , 10 cm and 18 cm in diameter centered in the FOV. With an initial activity

concentration of 50  $\mu\text{Ci}/\text{cc}$ , the cylinders were scanned in 3-min frames for 15 half-lives at LLD settings of 250, 350, and 450 keV.

### Resolution

The intrinsic transaxial resolutions were determined from the block response measurements made with the  $^{22}\text{Na}$  line source (above). LLD settings of 250, 350 and 450 keV were used with the ULD set at 650 keV. Measurements of the reconstructed resolution (ramp filter) used the intrinsic data from the center out to 28 mm radius, with additional measurements at 20-mm intervals out to 12 cm. The axial resolution for direct and cross planes also was evaluated at each of these energy settings using the plane sensitivity data obtained above.

### Detector Uniformity

The effect of spillover in the block was determined by measuring the relative sensitivity and intrinsic coincidence pair resolution of each crystal in a block. Significant variations in sensitivity across the face of a block will lead to problems with normalization, increased image noise, and ultimately, artifacts in the reconstruction (9). We measured the worst-case variations of both sensitivity and resolution using the block response data described earlier. At each energy setting, intrinsic FWHM variations and relative coincidence efficiencies were evaluated for each crystal from the intrinsic LSFs.

### Event Positioning

A lucite phantom consisting of line sources both parallel and oblique to the axis of the tomograph was used to measure the net misplacement of the data throughout the imaging volume. Transaxial images through the phantom are a series of dots whose centroids may be used to determine the three-dimensional positioning accuracy of reconstructed data. The phantom was filled with 5 mCi of  $^{18}\text{F}$  and scanned 10 times for variable time frames ranging from 15 to 60 min to compensate for decay. Images were reconstructed with a ramp filter to a 256 matrix for more precise localization of the image dots. After correcting for radial mispositioning due to geometrical and parallax effects (10), the images were analyzed to determine the axial mispositioning of each point in the image volume.

The macroscopic effect of a deliberately misplaced axial detector boundary was measured using a modified algorithm for defining the position LUT (see Fig. 7). The modification was expected to spill events from direct planes (n) into planes (n+1) in one half of the block, causing a shift in the position of planes 10 through 15. Identical data sets were acquired following both correct and incorrect calibrations of the position LUTs in all blocks.

### Scatter

A single  $^{68}\text{Ge}$ - $^{68}\text{Ga}$  line source was placed at various radial positions in 10-cm and 18-cm diameter cylinders and sinograms were obtained for each position. Events in the peak of the line source were assumed to be unscattered and those in the tails and under an interpolated line spanning the peak were assumed to be scattered. Each line source was used to measure the scatter fraction for an annular region of the cylinder, which was then used to calculate a weighted average representing the scatter in an equivalent uniform cylinder of activity. Since the front-end electronics in this tomograph also allow dual-window measurement of the scatter, line source data were acquired using energy windows of 150–350 keV and 350–650 keV.

### Energy Discrimination

The effect of crystal-specific energy discrimination was determined using the data acquired in the above sections by measuring scatter fraction, intrinsic transaxial resolution, and axial resolution as a function of energy window.

## RESULTS

### Sensitivity

Table 2 summarizes the sensitivity measurements of the 713 as measured with a uniform 20-cm cylindrical phantom. Sensitivity and count rate performance were also measured at three LLD settings over a wide range of activities with both the 10-cm and 18-cm diameter cylinders. In order to provide more insight into the relative usefulness of the system at high count rates, noise equivalent counts (NECs) (11) were also calculated from this data with the following equation:

$$\text{NEC} = \frac{T^2}{T + S_i + 2R_i}$$

where T,  $S_i$ , and  $R_i$  are the true, scattered and random coincidence rates, respectively. The randoms and scatter include only those events lying under the 10-cm or 18-cm diameter object. Plots of the results of these calculations as well as plots of the true and random rates of both cylinders are shown in Figure 4.

In Figure 5, the effect of using enhanced direct planes in order to improve sensitivity is illustrated. Plots of the axial LSFs for both the standard and sensitivity-enhanced plane configurations are shown. A factor of 2 greater sensitivity of the cross planes compared to the direct planes in the standard configuration is evident in Figure 5a. The enhanced configuration reduces this disparity but at the cost of poorer axial resolution towards the edge of the FOV.

### Resolution

Figure 5 also demonstrates the axial resolution of the system. The FWHM values are determined by linear interpolation between the 0.75-mm samples and an average of all equivalent planes. The standard configuration in Figure 5a shows little change in the plane thickness with position in the FOV. The sensitivity enhanced configuration in Figure 5b has axial resolution comparable to the standard configuration at the center but shows a significant loss of resolution at a 10-cm radius.

**TABLE 2**  
Summary of Low Count Rate Sensitivity Measurements

Sensitivity (kcps/ $\mu\text{Ci}/\text{cc}$ )	250 keV	350 keV	450 keV
Direct plane	2.18	1.88	1.37
Cross plane	4.19	3.54	2.56
Enhanced plane	6.08	5.17	3.65
System—Standard	46.8	39.8	28.9
System—Enhanced	68.6	58.1	41.8

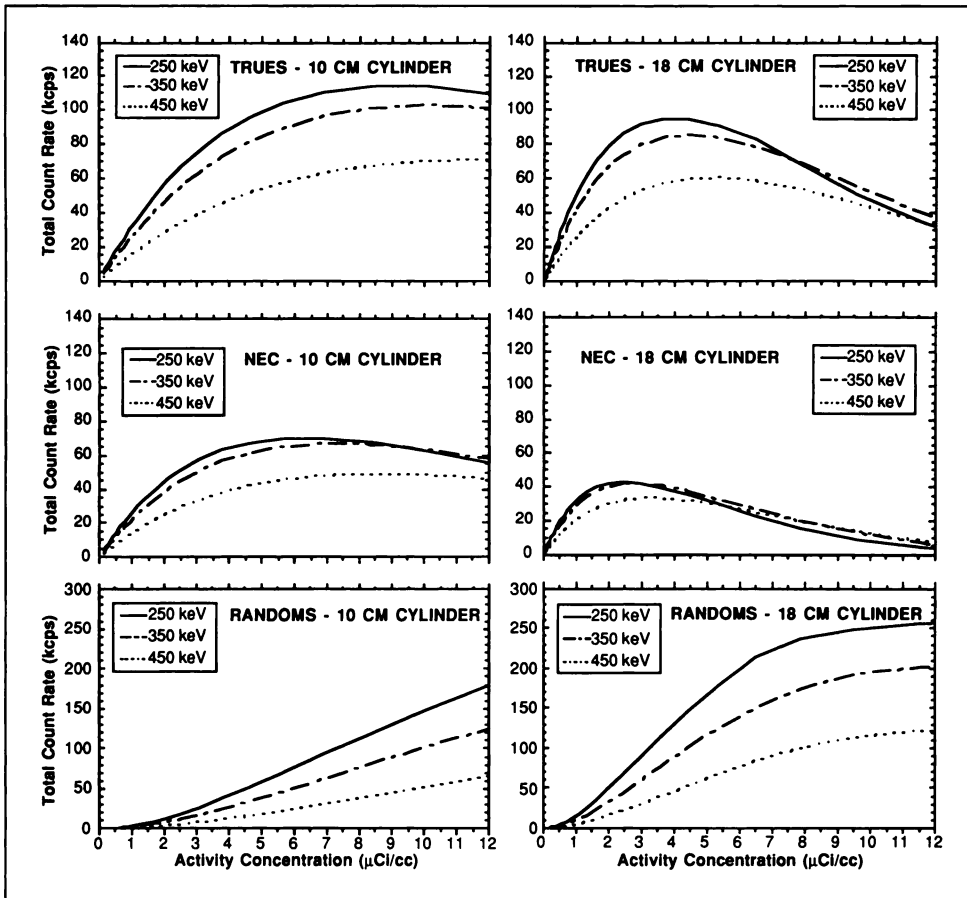


**FIGURE 4.** Saturation count rate measurements using  $^{18}\text{F}$  in 10 cm and 18 cm diameter cylinders. Frames of 3 min duration, separated by a 30-min delay and using three different energy thresholds, were acquired from the decaying cylinder. Trues, noise equivalent counts, and randoms are plotted at three different energy settings. All measurements were obtained with the enhanced plane configuration.

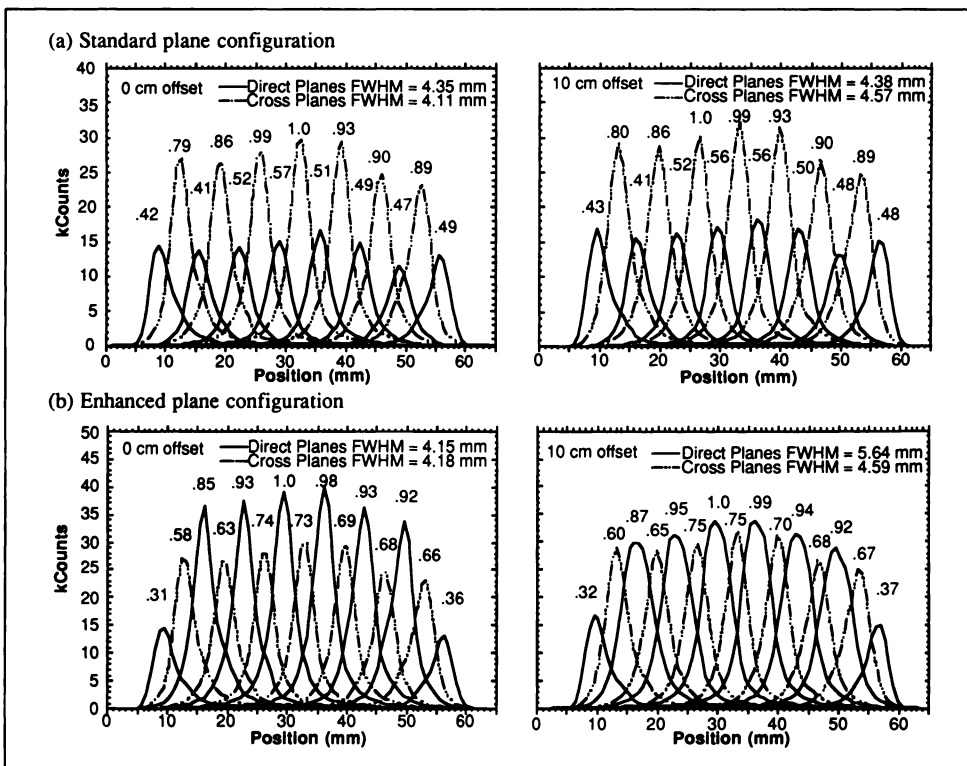


**FIGURE 5.** Axial line spread functions for the (a) standard and (b) high-sensitivity plane configurations at the center and near the edge of the FOV. When compared with the standard configuration, the enhanced configuration has more uniform plane sensitivity, although some degradation of the axial resolution is evident at the edge of the FOV. Normalized sensitivities are indicated for each plane.

**FIGURE 6.** Intrinsic and reconstructed spatial resolution at 450 keV. (a) Transaxial LSFs covering a single pair of blocks in coincidence were acquired by sweeping a narrow line source across the coincidence region and extracting the non-normalized counts from the sinogram. Shown are the FWHM values and the relative coincidence efficiencies of each crystal. (b) Reconstructed image resolution across the useful FOV was determined from an interpolated profile through a reconstructed line source (ramp filter). The oscillating response near the center is an artifact of the radial sampling.

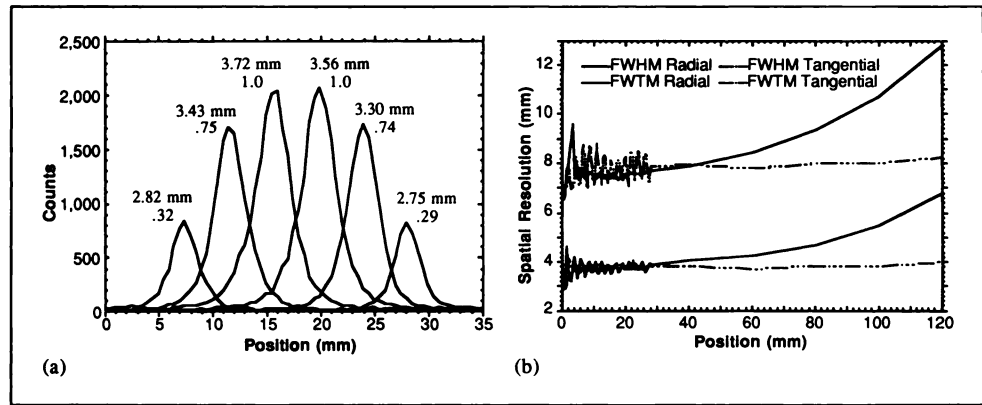


Figure 6 shows the results of the intrinsic and reconstructed transaxial resolution measurements at 450 keV. Average intrinsic resolutions for all energies are tabulated in Table 3, and reconstructed transaxial resolution (ramp filter) is shown in Figure 6b. Radial sampling effects are evident near the center of the FOV where the line source was stepped in 0.5-mm increments. The radial component of the FWHM rises from roughly 3.8 mm at the center to 6.7 mm at 12 cm radius due to detector penetration and geometric effects, while the tangential component remains constant at 3.8 mm.

### Detector Uniformity

Figure 6a also shows significant variation in resolution and relative sensitivity among the crystals in a block. Edge crystals are only 30% as efficient as the center crystals at 450 keV, while fractions of 55% and 49% were measured at thresholds of 350 and 250 keV, respectively. These effects are partly due to interdetector spillover and partly due to the fact that the edge crystals are slightly narrower (3.25 mm) in order to pack them into the gantry. Edge crystals typically have 20%–25% better spatial resolution due to lower spillover effects and their smaller size.

**TABLE 3**  
Parameters Particularly Affected by Energy Threshold

	250 keV	350 keV	450 keV
Scatter fraction	19/33%	16/26%	10/13%
Avg. intrinsic resolution (mm)	3.6 (8.9)	3.5 (8.4)	3.3 (7.3)
Avg. axial resolution (mm)	4.9/4.5	4.9/4.3	4.6/4.2

Scatter as a fraction of true events in 10/18 cm phantoms. Intrinsic resolution values are FWHM (FWTM), averaged for three block pairs at the center of the tomograph. Axial resolution is indicated for enhanced direct/cross planes as an average of values at 0 and 10 cm radius.

### Event Positioning

Figure 7 illustrates the effect of using positioning LUTs with incorrectly placed axial plane boundaries. Figure 7a shows the detector positioning histograms overlaid by the LUT boundaries for a detector that was calibrated properly. Figure 7b shows a set of boundaries that could result if the detector were calibrated improperly. The bar graph in Figure 7c shows the error in the plane position

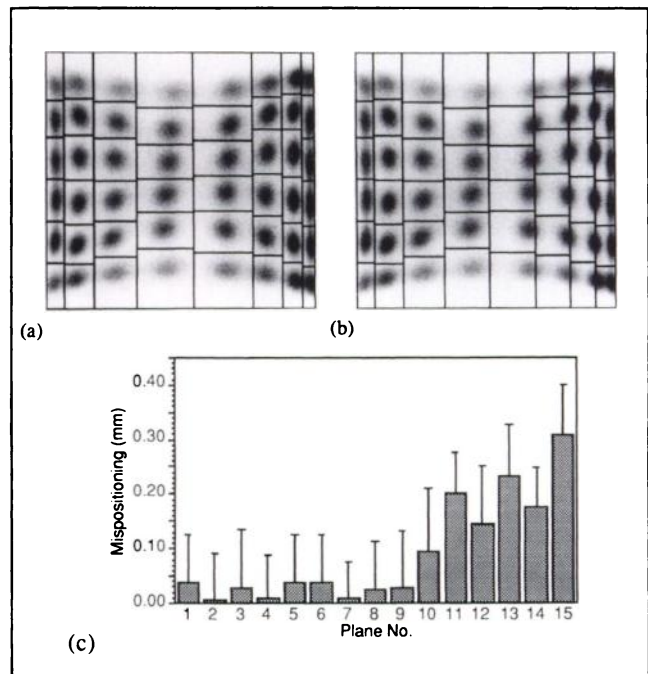


**FIGURE 7.** Axial mispositioning from incorrectly placed boundaries in the position LUT. A deliberate error in the setup algorithm caused boundaries to be shifted in the right half of the block (b). The plot in (c) is the resulting axial mispositioning of planes 10 through 15, corresponding to the incorrect axial boundaries in (b). Plane positions are determined from reconstructed images of oblique line sources.

that is caused by the LUT in Figure 7b. Error bars were determined by repeated measures of the plane positions with all detectors calibrated properly. The centroids of the oblique line sources in the phantom indicate the plane positions as previously described. Some of the events striking the right side of the block in Figure 7b will be incorrectly placed in the column to the right due to the error in the boundaries separating these columns. Thus, events are spilled from planes 13 and 14, for example, into plane 15. This effect will not be noticeable if the error occurs in only a single block. In this case, however, the boundary was deliberately placed incorrectly in all blocks by manipulating the LUT algorithm. The result is a slight decrease in spacing for planes 10 to 15 and a shift toward the center of the axial FOV.

### Scatter

For a 24-cm FOV, the scatter fractions in an 18-cm diameter cylinder using LLD values of 250, 350, and 450 keV were found to be 0.33, 0.26 and 0.13, respectively. The 10-cm diameter cylinder had scatter fractions of 0.19, 0.16 and 0.10 for the corresponding LLD values. The relevant scatter fraction when considering signal to noise ratio is that from the fraction of the FOV which is beneath the object. The scatter fractions are reduced by 14% and 31% (at 350 keV), if only the areas under the 18- and 10-cm diameter object, respectively, are considered.

Acquisition of data with a dual energy window provides the possibility of a measured scatter correction. A photopeak window of 350–650 keV is used while data are simultaneously acquired in a scatter window, 150–350 keV. The count rates in a typical pair of sinograms differ by a factors of 4–5 in magnitude with the distribution of events appearing very similar. The scatter window distribution resembles a slightly smoothed version of the photopeak data. This indicates that many of the apparently low energy events are unscattered. These are events that have escaped the source without scattering but are only partially absorbed by the detector. They are correctly placed but deposit only a fraction of their energy in the detector and therefore fall into the scatter energy window.

### Energy Discrimination

Tables 2 and 3 list energy-sensitive parameters for LLD values of 250, 350, and 450 keV. Scatter, spatial resolution and count-rate performance change significantly with energy threshold, showing the effectiveness of energy-based event rejection with the digital electronics. Intrinsic resolution benefits from energy-based rejection of multi-crystal events. FWHM improves by 12% and FWTM by 20% when the threshold is raised from 250 to 450 keV. The fact that the improvement is greatest for the center crystals, especially at the FWTM level, is an indication that inter-detector spillover is a significant factor in resolution.

Axial resolution for enhanced direct and cross planes is averaged from measurements at 0 and 10 cm radius. Similar response to energy threshold is seen with these

measurements although the inter-plane spillover is less pronounced than in the transaxial direction due to the larger crystal dimension in the axial direction.

Count rate performance (Fig. 4, Table 2) has the expected relationship with energy threshold. The true count rate is higher for lower thresholds at all activities up to the saturation point. At saturation, the peak of the true count rate occurs at a higher activity concentration for higher thresholds. Useful counts, as indicated by the NEC curve, are virtually the same for the 250 and 350 keV thresholds at higher count rates.

### Images

Figures 8–10 illustrate the imaging performance of the system with animals and man. Figure 8 is an anesthetized Nemistrina monkey imaged for 90 min after a 10-mCi injection of  $^{18}\text{F}$ FDG. Contrast between gray and white matter is significantly less than in a human subject (Fig. 9), since the monkey's white matter consists of very narrow strips (1–2 mm) separating the cortex from the sub-cortical gray matter. Figure 9 shows a comparable  $^{18}\text{F}$ FDG study of a normal volunteer following a 10-mCi injection and 40 min of uptake. Data were acquired for 120 min because of the low sensitivity of the individual planes as compared to clinical PET systems. Figure 10 is a whole-body acquisition of a normal dog following a 10 mCi dose of  $^{18}\text{F}$ FDG (left) and 10 mCi of [ $^{18}\text{F}$ ]flouride ion (right).

### DISCUSSION

The slice thickness of the 713 is essentially one-half that of its predecessor, the CTI 831/12-08, which has an identical detector ring diameter (12). The geometric sensitivity of a 713 direct plane should be 25% of an 831 direct plane (solid angle reduced 50% and activity viewed by detector pair reduced 50%). Taking these geometric differences into account, the measured direct plane sensitivity for the 713 is only 75% of the expected value. This shortfall is likely a result of the small crystal size of the 713. It was realized

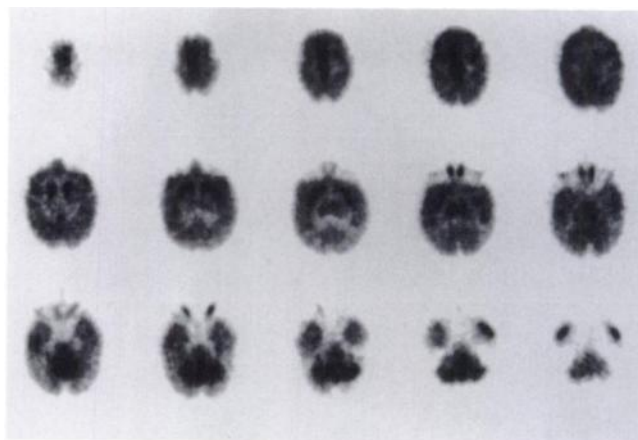


**FIGURE 8.** Fluorine-18-FDG images of a Nemistrina monkey after 10 mg/kg ketamine injection. Image planes were acquired in 90 min with an energy window of 350 to 650 keV. The brain is 5.5 cm across by 6.0 cm a-p by 4.8 cm tall.

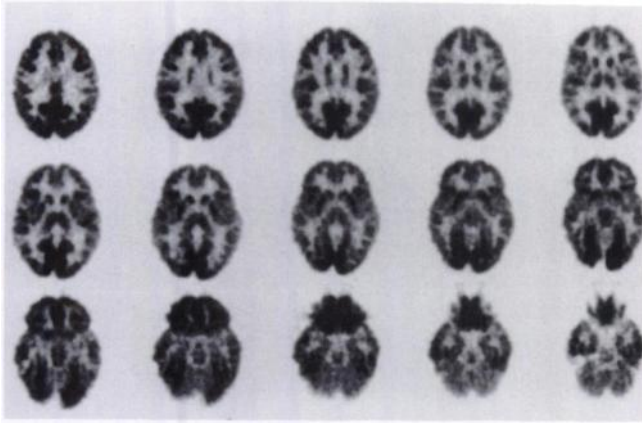


**FIGURE 9.** Fluorine-18-FDG images of a normal volunteer. Images were acquired in 120 min following 40 min of uptake. The system is not designed to handle the scatter from an adult human head (~26% in these images). This study is shown here for comparison.

that the system sensitivity could be marginal, therefore the interplane septa were reduced (in length from 16 to 6 cm and in thickness from 1 to 0.5 mm) to compensate for the direct plane losses with additional crossplane events. Still more oblique events were recruited with the implementation of the enhanced direct plane data collection mode. The improvement in sensitivity which results, however, is larger than expected, indicating a significant fraction of septal penetration. While potentially problematic in human subjects, the septal penetration as well as the additional scatter due to the open geometry are more tolerable effects for a system dedicated to imaging small animals since the ratio of scatter to trues is much smaller.

These modifications improved the overall sensitivity of

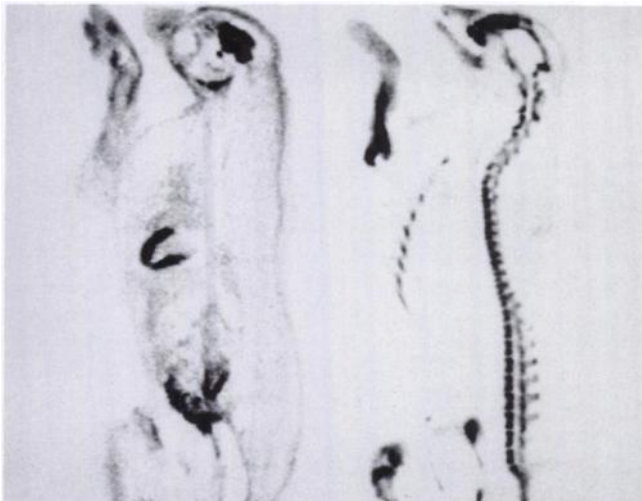


**FIGURE 10.** Whole-body images of a normal dog following 10 mCi of  $^{18}\text{F}$ FDG (left) and 10 mCi of  $[^{18}\text{F}]$ fluoride ion (right). Data were acquired at 32 different positions of the tomograph bed. The assembled volume of image data consists of 480 transaxial planes which are resliced into these coronal views after some axial smoothing.

the system (Table 2) to an acceptable level and provided some improvement in the uniformity of plane sensitivity (Figure 5). The effect of the shorter/thinner septa becomes evident in the comparison of the count rate data for the 10- and 18-cm cylinders. The 18-cm cylinder with its larger scatter fraction has a significantly poorer deadtime performance than the 10-cm cylinder (Fig. 4). Plots for the 10-cm cylinder demonstrate much better performance in all the count rate categories with the system saturating at over 100K trues/sec for this single 5-cm ring of detectors. The 10-cm cylinder provides a scatter environment similar to that seen in primate studies, while the 18-cm cylinder approximates the scatter from the thorax of a dog or a human head.

Nonuniform sensitivity in this modular detector is more pronounced than in earlier designs. The small crystal dimensions of this detector apparently account for the greater variation in performance among crystals in a block, as evidenced by the more uniform response of a similar block with 6-mm detectors (13). Interactions in an edge crystal that scatters have a good chance of escaping the block and being rejected by energy discrimination. However, similar events near the center of an array of 3-mm crystals usually result in the absorption of the scattered photon in an adjacent crystal (14). These multi-crystal interactions will still satisfy the position and energy requirements for a valid event, and their acceptance causes a loss in image resolution. A greater problem, however, arises from the variation in sensitivity which also results from this effect. Large variations in sensitivity across the block which are subsequently removed by detector normalization result in an enhanced level of noise in reconstructed images (9). This modulating block sensitivity becomes worse as the energy threshold is increased. Relatively poor optical coupling of crystals at the edge of the block gives rise to poor energy resolution (FWHM~30%) compared with crystals in the center of the block (FWHM~20%). This means, that at thresholds as low as 350 keV, events in the photopeak are being lost due to energy discrimination.

Thus, Compton scatter within the block appears to be a primary factor in degrading spatial resolution when compared to discrete detectors of the same size. Single detectors of BGO would be expected to produce intrinsic coincidence pair resolution of approximately 2.6 mm FWHM, considering detector size, non-collinearity, and positron range. The intrinsic resolutions of edge crystals in this block, which record fewer multi-crystal interactions, are very close to this value (2.7–2.8 mm FWHM), while central crystals have nearly 25% poorer resolution (3.3–3.7 mm FWHM). Reconstructed resolution is within 15% of average intrinsic resolution at all energies, with the loss due to under-sampling and statistical bias of the filtered back projection algorithm. Detector penetration is significant, as illustrated by the step fall-off in reconstructed FWHM in Figure 6. This effect is mitigated by the large

ring diameter compared with other systems dedicated to animal studies (15).

The accuracy of data placement is illustrated in Figure 7. The resolution of the system is on the order of 4 mm, but the plane positions, determined from the centroids of transaxial LSFs, are seen to be reproducible to about  $\pm 0.1$  mm. This means that there is very little gross spatial distortion in the data after correction for the geometric and detector penetration effects that are common to all circular PET systems. With the event position discrimination dependent on a system of software-defined detector boundaries, the possibility of systematic mispositioning of the data was felt to be worthy of investigation. Errors in the setup algorithm, pile-up due to high data rates during calibration, amplifier and PMT gain shifts can all cause significant mispositioning of the detector boundaries. In terms of the practical operation of the system, however, it is seen that a deliberate miscalibration of the system causes less than 0.5-mm error in data positioning in the axial direction. This implies that basic data quality is not critically sensitive to system operating parameters and that problems such as modest drift of the electronics or occasional neglect of calibration should not seriously affect the results of studies.

The use of the second energy window provides data resembling a scatter distribution contaminated with true coincidence events. These partially absorbed events present a problem unique to PET, which was not a consideration in the original application of this technique to scatter correction in SPECT (16). The contamination of trues in this window requires a method to remove the trues from the scatter window. In addition, the scatter in the low energy window is primarily large-angle scatter while the scatter in the true coincidence window is primarily small-angle scatter. These distributions are different and a relationship must be developed between them if one is to be used to correct for the other. While the implementation of a scatter correction with the second energy window may not be simple, the additional information has the potential of providing a correction based on a measurement rather than an idealized model of the process.

Figures 8 through 10 provide illustrations of the image quality attainable with the 713. The FDG images of the normal volunteer (Fig. 9) were included to provide a point of reference for the system, since the FDG metabolic scan is the most common procedure performed with PET today. The detail and contrast are very good for a multislice PET camera, despite the high scatter content. Unfortunately, due to the low sensitivity per plane, it required 120 min of scanning time to achieve this level of image quality. The delineation of cortical and sub-cortical gray structures in the primate study (Fig. 8) was poorer than originally anticipated. However, reconsideration of the experimental conditions and the anatomy of the non-human primate indicate that the results are reasonable. First, the animal was injected and scanned under anesthesia, which globally

reduces cortical metabolism and therefore reduces contrast between gray and white matter. Second, the proportion of white matter in the primate brain is much smaller than in man. The white matter consists primarily of narrow (1–2 mm) strips between cortical and central gray structures. Both of these factors are consistent with the images in Figure 8.

The whole-body images of [ $^{18}\text{F}$ ]FDG and [ $^{18}\text{F}$ ]fluoride ion shown in Figure 10 illustrate a type of study that will be important in the application of the CTI 713 to basic radiopharmaceutical development. The biodistribution of new radiopharmaceuticals will be an important first step in assessing the usefulness of a new compound for clinical or research applications. Biodistribution in primates also will be important in assessing the radiation dosimetry of a compound before its application to human subjects.

## CONCLUSION

The CTI/Siemens 713 Animal Tomograph has demonstrated good overall performance in imaging a wide variety of animals with many different tracers. Its performance is degraded, however, when imaging objects larger than those for which it was designed, a human head or chest for example. In particular, the scatter and randoms fractions under these conditions are higher than practical for quantitative imaging. The 40-cm diameter aperture is adequate for large dogs, but even a moderately large human thorax will not fit. Fifteen contiguous slices with image and axial resolutions of 4 mm FWHM can be realistically achieved in static images with  $^{18}\text{F}$ -labeled compounds and only slightly poorer resolution with  $^{11}\text{C}$ - and  $^{13}\text{N}$ -labeled compounds. While other systems may have somewhat better image resolution, the improved axial resolution and contiguous slices of this system provide volumetric data with uniform spatial resolution. This greatly simplifies experimental setup and allows data to be resliced as an aid for data analysis and presentation. The changes to this system are confined to the detector and front-end electronics. Hence, the software is basically the same as for previous CTI systems—sinogram size and a few physical parameters are different. This means that all previous display and data analysis software designed for CTI's clinical PET systems can be used with the data from the 713 without further development or modification.

The digital front-end electronics of the system provides the means to deal adequately with the problems of non-uniform signal amplitude from the various detector elements and the non-linearities in the crystal identification signals as reflected by the curvature of the vertical rows in Figure 3. Earlier versions of the block with analog electronics made use of voltage comparators with step-wise reference voltages to discriminate the position of each event. This made the detector boundaries effectively a rectangular grid with no means to compensate for the nonlinearities inherent in the block. Average energy thresholds for the inner and outer crystals have been

replaced by unique values for each crystal. The new system allows optimal position and energy parameters to be determined and saved with each calibration of the detector.

For this study, the system was operated with the default LUTs provided. In addition, the enhanced direct planes were added as a data collection option. Future modifications include:

1. A system design that allows the creation of custom positioning LUTs, such as those shown in Figure 3, thereby minimizing the acceptance of ambiguous events. Custom energy LUTs may also be implemented to compensate for differences in detector element efficiencies.
2. Different cross-plane combinations (such as the enhanced direct plane) that can be tested and the inter-plane septa removed for full three-dimensional collection.
3. A second energy window that can be investigated as a means of scatter estimation and correction.

#### ACKNOWLEDGMENTS

The authors thank R. Sumida, J. Edwards, and H. Hansen for technical support and N. Satyamurthy for preparation of radiopharmaceuticals. This work was supported by Department of Energy Contract DE-FC03-87ER 60615 and National Institutes of Health grants R01-MH37916 and P01-NS15654.

#### REFERENCES

1. Derenzo SE, Huesman RH, Cahoon JL, et al. A positron tomograph with 600 BGO crystals and 2.6 mm resolution. *IEEE Trans Nucl Sci* 1988;33:659-664.

2. Casey ME, Nutt R. A multicrystal two-dimensional BGO detector system for PET. *IEEE Trans Nucl Sci* 1986;33:460-463.
3. Dahlbom M, Hoffman EJ. An evaluation of a two-dimensional array detector for high-resolution PET. *IEEE Trans Med Imag* 1988;7:264-272.
4. Digby WM, Dahlbom M, Hoffman EJ. Detector, shielding and geometric design factors for a high resolution PET system. *IEEE Trans Nucl Sci* 1990;37:664-670.
5. Hoffman EJ, Ricci AR, Van der Stee LMAM, Phelps ME. ECAT III—basic design considerations. *IEEE Trans Nucl Sci* 1983;30:729-733.
6. Moyer JC. A high performance detector electronics system for positron emission tomography. Master of Science thesis, University of Tennessee, Knoxville 1990.
7. Spinks TJ, Jones T, Gilardi MC, Heather JD. Physical performance of the latest generation of commercial positron scanners. *IEEE Trans Nucl Sci* 1988;35:721-725.
8. Dent HM, Jones WF, Casey ME. A real time digital coincidence processor for positron emission tomography. *IEEE Trans Nucl Sci* 1986;33:556-559.
9. Cutler PD, Hoffman EJ. Use of digital front-end electronics for optimization of a modular PET detector. *IEEE Nuclear Science Symposium*, Santa Fe, NM, 1991.
10. Hoffman EJ, Guerrero TM, Germano G, Digby WM, Dahlbom M. PET system calibration and corrections for quantitative and spatially accurate images. *IEEE Trans Nucl Sci* 1989;36:1108-1112.
11. Strother SC, Casey ME, Hoffman EJ. Measuring PET scanner sensitivity: relating count rates to image signal-to-noise ratios using noise equivalent counts. *IEEE Trans Nucl Sci* 1990;37:783-788.
12. Hoffman EJ, Digby WM, Germano G, Mazziotta J, Huang SC, Phelps ME. Performance of a neuroPET system employing 2-D modular detectors. *J Nucl Med* 1988;29:983-984.
13. Evans AC, Thompson CJ, Marrett S, Meyer E, Mazza M. Performance evaluation of the PC-2048: a new 15 slice encoded-crystal PET scanner for neurological studies. *IEEE Trans Med Imag* 1991;10:90-98.
14. Derenzo SE. Monte Carlo calculations of the detection efficiency of NaI(Tl), BGO, CsF, Ge, and plastic detectors for 511 keV photons. *IEEE Trans Nucl Sci* 1981;28:131-135.
15. Tomitani T, Nohara N, Murayam H, Yamamoto M, Tanaka E. Development of a high resolution positron CT for animal studies. *IEEE Trans Nucl Sci* 1985;32:822-825.
16. Jaszczak RJ, Greer KL, Floyd CE, Harris CC, Coleman RE. Improved quantitation in SPECT using compensation for scattered photons. *J Nucl Med* 1984;25:893-900.